Electronic Supplementary Information

Defects Engineered Metal-Organic Frameworks for Volumetrically and Kinetically Co-Enhanced Atmospheric Water Harvesting†

Qingling Fu,[a] Dong Liu,[e] Jianwei Yang,[a] Yehao Jin,[a] Zhibing Sun,[c] Chunyu Liu,[a] Yuze Sun,[a] Chao Sun,[a] Qianyou Wang*[b,c] and Qinglang Ma*[a,c,d,e]

[a]Frontiers Science Center for High Energy Material, Advanced Research Institute of Multidisciplinary Science, Beijing Institute of Technology, Beijing 100081, China.
[b]State Key Laboratory of Explosion Science and Technology and Safety Protection, Beijing Institute of Technology, Beijing 100081, China.
[c]Beijing Institute of Technology, Zhengzhou Academy of Intelligent Technology, Zhengzhou 450000, China.
[d]Beijing Institute of Technology, Chongqing Innovation Center, Chongqing 401120, China.
[e]Chongqing Advanced Materials Institute, Chongqing 408107, China.
E-mail: qinglangma@bit.edu.cn (Q. Ma); qianyouwang@bit.edu.cn (Q. Wang)

Table of Contents

1. Structural characterization

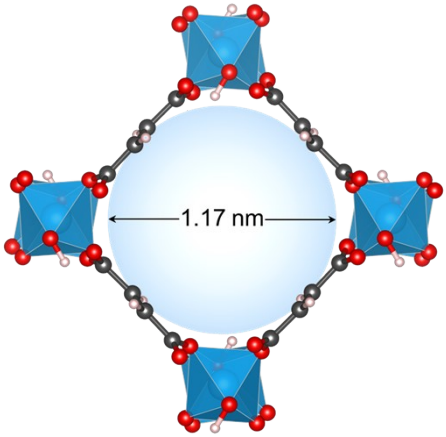

Fig. S1. The pore size of Al-Fum based on its simulated structure.

Note S1：

The calculation formula is as follows:

The oxidized products of Al-Fum under thermogravimetric analysis in air are solid alumina and other gaseous products, as represented by the following equation:

$$AlOH(C_4O_4H_2) + 3O_2 = 0.5Al_2O_3 + 4CO_2 + 1.5H_2O$$

Thus, the measured remaining mass ratio after TGA is attributed to the solid Al_2O_3. In addition, the OH and H2O species exit in pairs to maintain both the charge and the coordination number. Based on the experimentally obtained residual mass ratio (Rexp) of Al_2O_3 obtained from the TGA analysis, which is the experimental MOF/Residue ratio. The general formula of defective Al-Fum can be written as $Mw(AlOH(C_4O_4H_2)_X(OH/H_2O)_{1-X}$, in which the residual ligand content (X) in the molecular composition of defective Al-Fum can be calculated using the following equation.[1]

$$X = \frac{R_{exp} * 0.5 * M_w(Al_2O_3) - M_w(AlOH) - M_w(OH/H_2O\ pair)}{M_w(C_4O_4H_2) - M_w(OH/H_2O\ pair)}$$

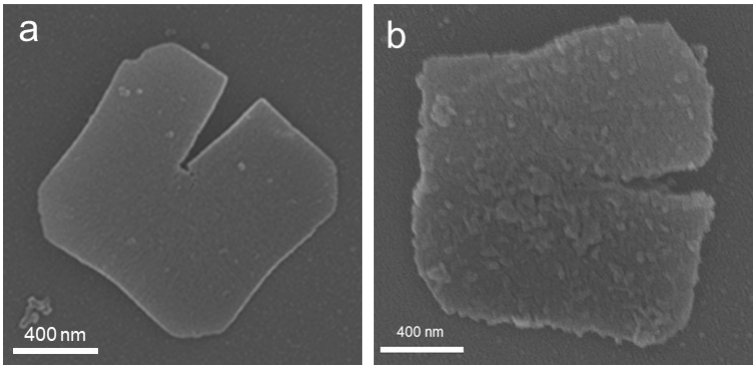

Fig. S2. SEM image of (a) Al-Fum, (b) D-Al-Fum.

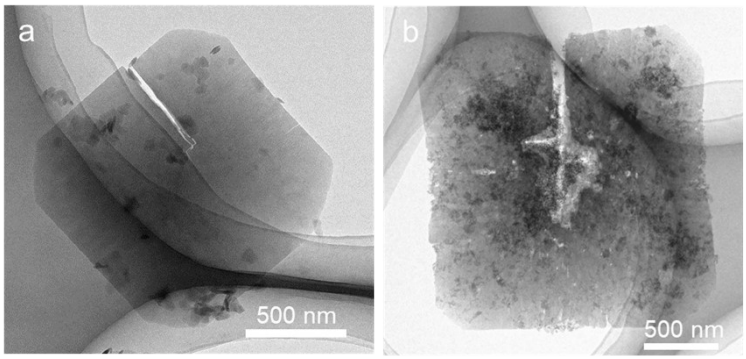

Fig. S3. TEM image of (a) Al-Fum, (b) D-Al-Fum.

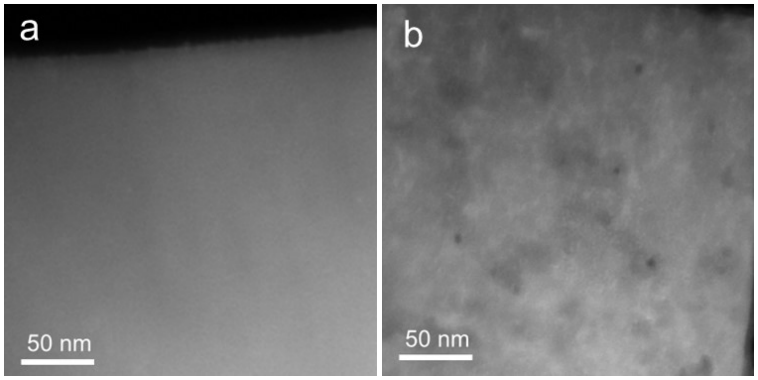

Fig. S4. HAADF-STEM image of (a) Al-Fum, (b) D-Al-Fum.

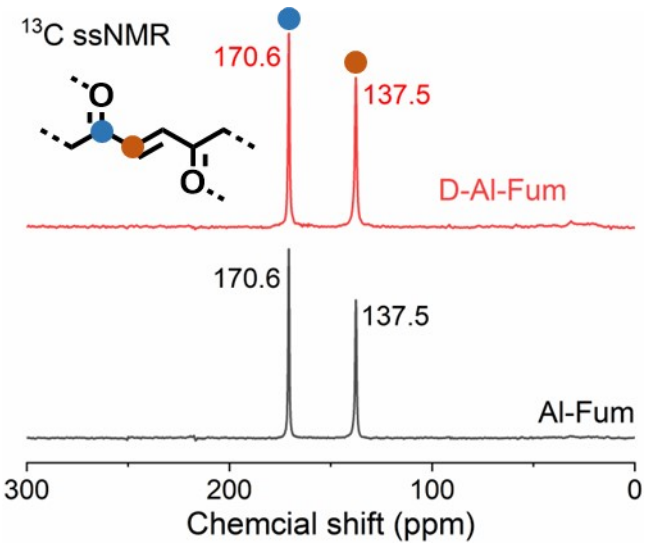

Fig. S5. Solid-state ^{13}C CP/MAS ssNMR spectra of Al-Fum (black) and D-Al-Fum (red).

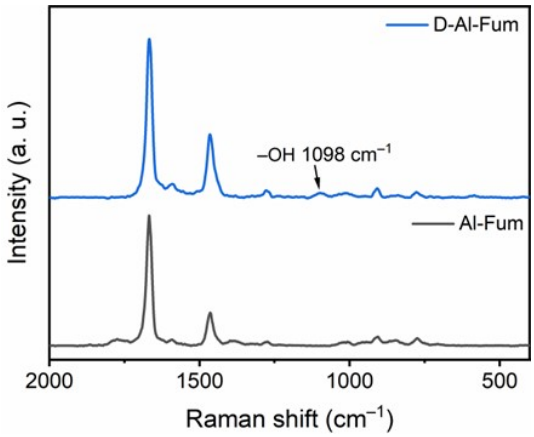

Fig. S6. Raman spectra of Al-Fum (black) and D-Al-Fum-(blue).

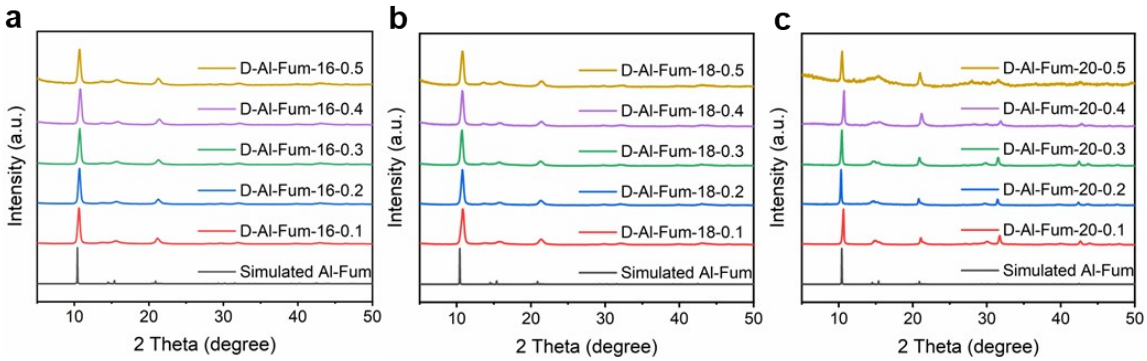

Fig. S7 Experimental and simulated PXRD patterns for series of defected Al-Fum.

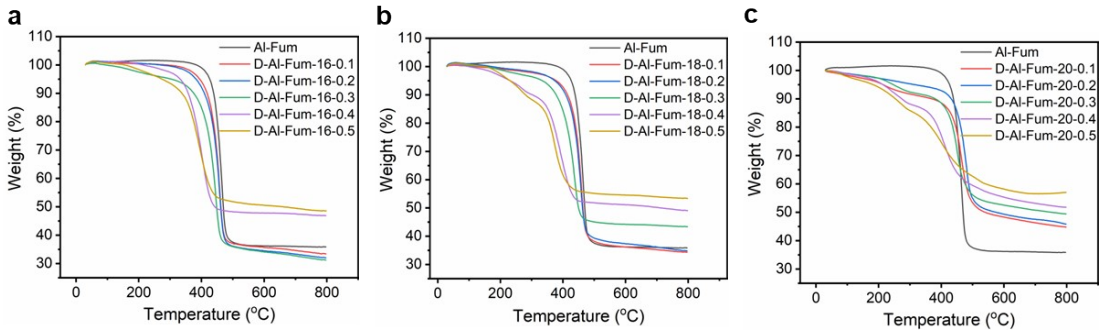

Fig. S8. TGA analyses of the series of defected Al-Fum.

Table S1. Calculated chemical formular of defective Al-Fum etched for 16 h under various etchant concentrations.

Sample	C_{Na2CO3} (mol L^{-1})	t (h)	Chemical formular
D-Al-Fum-16-0.1	**0.1**	16	$AlOH(C_4O_4H_2)_{0.93}OH_{0.07}H_2O_{0.07}$
D-Al-Fum-16-0.2	**0.2**	16	$AlOH(C_4O_4H_2)_{0.74}OH_{0.26}H_2O_{0.26}$
D-Al-Fum-16-0.3	**0.3**	16	$AlOH(C_4O_4H_2)_{0.52}OH_{0.48}H_2O_{0.48}$
D-Al-Fum-16-0.4	**0.4**	16	$AlOH(C_4O_4H_2)_{0.38}OH_{0.62}H_2O_{0.62}$
D-Al-Fum-16-0.5	**0.5**	16	$AlOH(C_4O_4H_2)_{0.33}OH_{0.67}H_2O_{0.67}$

Table S2. Calculated chemical formular of defective Al-Fum etched for 18 h under various etchant concentrations.

Sample	C_{Na2CO3} (mol L^{-1})	t (h)	Chemical formular
D-Al-Fum-18-0.1	**0.1**	18	$AlOH(C_4O_4H_2)_{0.89}OH_{0.11}H_2O_{0.11}$
D-Al-Fum-18-0.2	**0.2**	18	$AlOH(C_4O_4H_2)_{0.86}OH_{0.14}H_2O_{0.14}$
D-Al-Fum-18-0.3	**0.3**	18	$AlOH(C_4O_4H_2)_{0.49}OH_{0.51}H_2O_{0.51}$
D-Al-Fum-18-0.4	**0.4**	18	$AlOH(C_4O_4H_2)_{0.32}OH_{0.68}H_2O_{0.68}$
D-Al-Fum-18-0.5	**0.5**	18	$AlOH(C_4O_4H_2)_{0.21}OH_{0.79}H_2O_{0.79}$

Table S3. Calculated chemical formular of defective Al-Fum etched for 20 h under various etchant concentrations.

Sample	C_{Na2CO3} (mol L^{-1})	t (h)	Chemical formular
D-Al-Fum-20-0.1	**0.1**	20	$AlOH(C_4O_4H_2)_{0.44}OH_{0.56}H_2O_{0.56}$
D-Al-Fum-20-0.2	**0.2**	20	$AlOH(C_4O_4H_2)_{0.41}OH_{0.59}H_2O_{0.59}$
D-Al-Fum-20-0.3	**0.3**	20	$AlOH(C_4O_4H_2)_{0.31}OH_{0.69}H_2O_{0.69}$
D-Al-Fum-20-0.4	**0.4**	20	$AlOH(C_4O_4H_2)_{0.25}OH_{0.75}H_2O_{0.75}$
D-Al-Fum-20-0.5	**0.5**	20	$AlOH(C_4O_4H_2)_{0.13}OH_{0.87}H_2O_{0.87}$

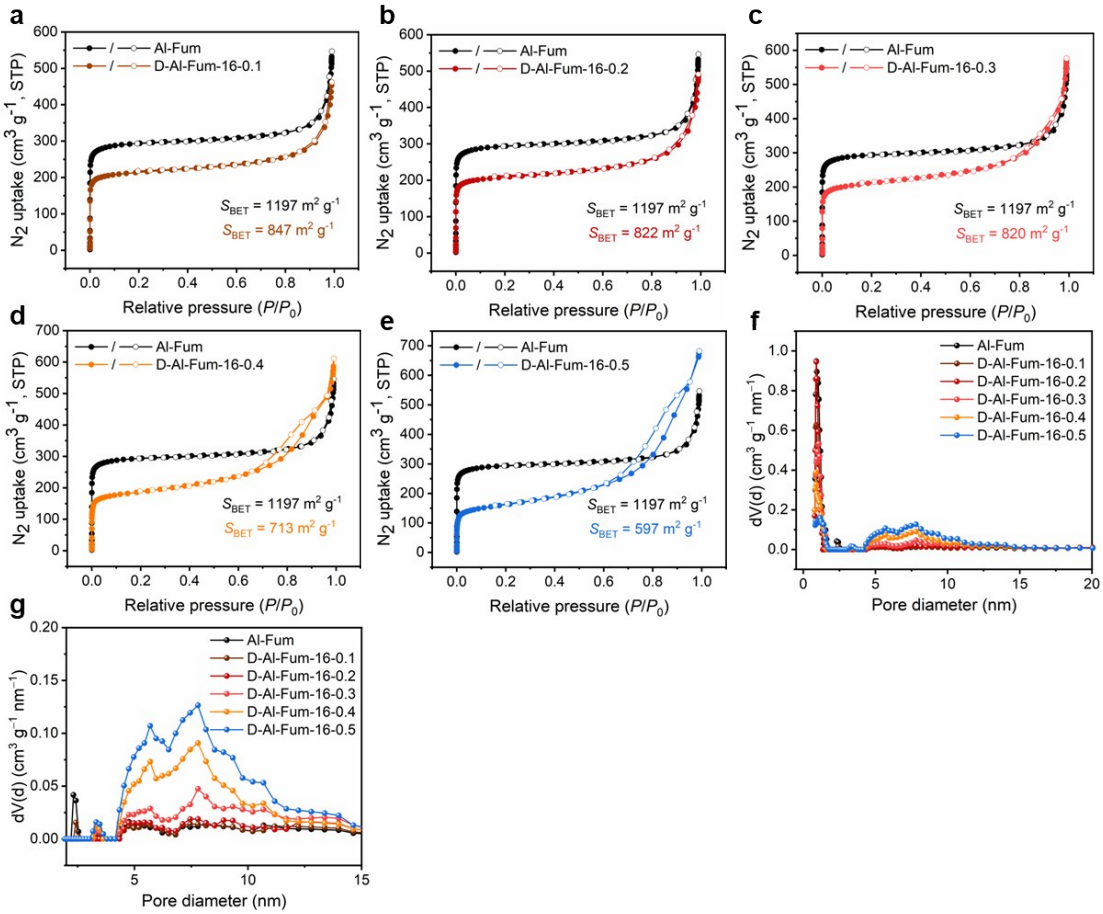

Fig. S9. Nitrogen adsorption-desorption isotherms and corresponding pore size distributions of (a) D-Al-Fum-16-0.1, (b) D-Al-Fum-16-0.2, (c) D-Al-Fum-16-0.3, (d) D-Al-Fum-16-0.4, (e) D-Al-Fum-16-0.5, (f) combined pore size distributions and (g) amplifications of the pore size distributions from 2 nm to 15 nm.

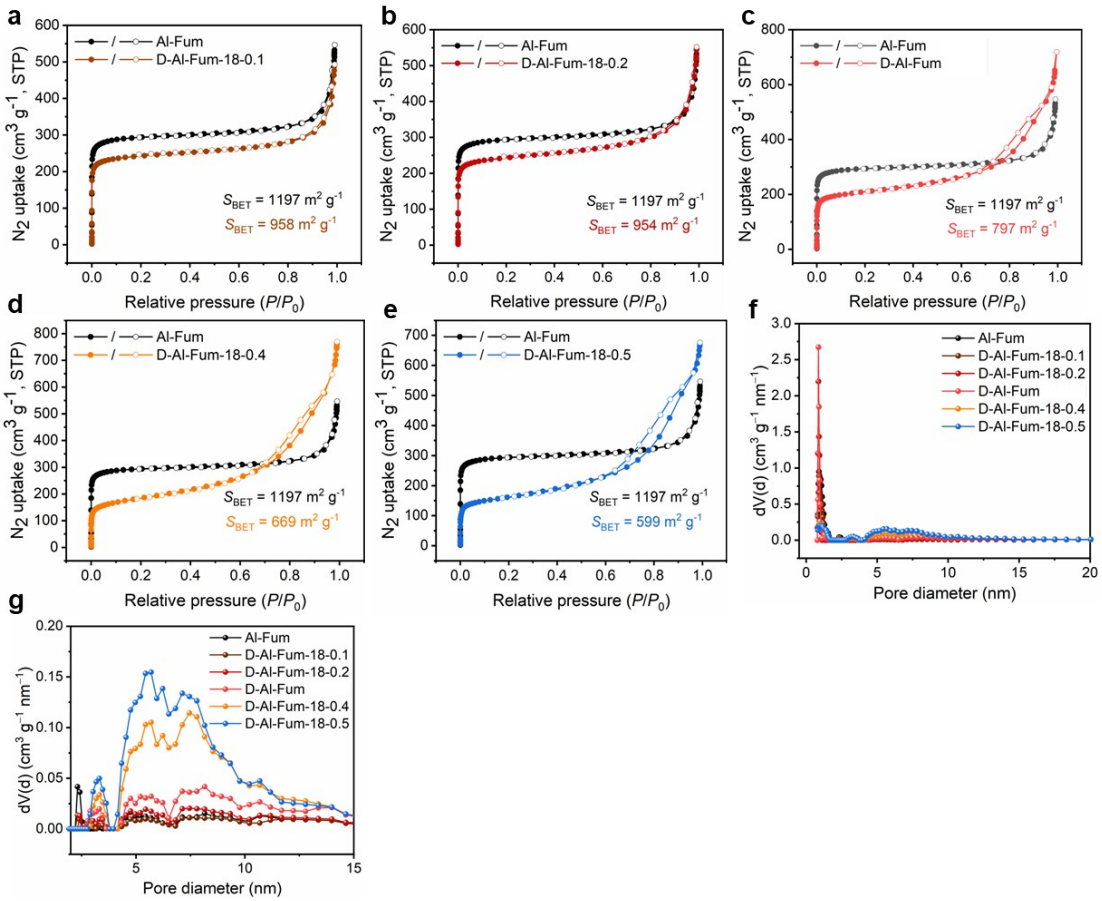

Fig. S10. Nitrogen adsorption-desorption isotherms and corresponding pore size distributions of (a) D-Al-Fum-18-0.1, (b) D-Al-Fum-18-0.2, (c) D-Al-Fum, (d) D-Al-Fum-18-0.4, (e) D-Al-Fum-18-0.5, (f) combined pore size distributions and (g) amplifications of the pore size distributions from 2 nm to 15 nm.

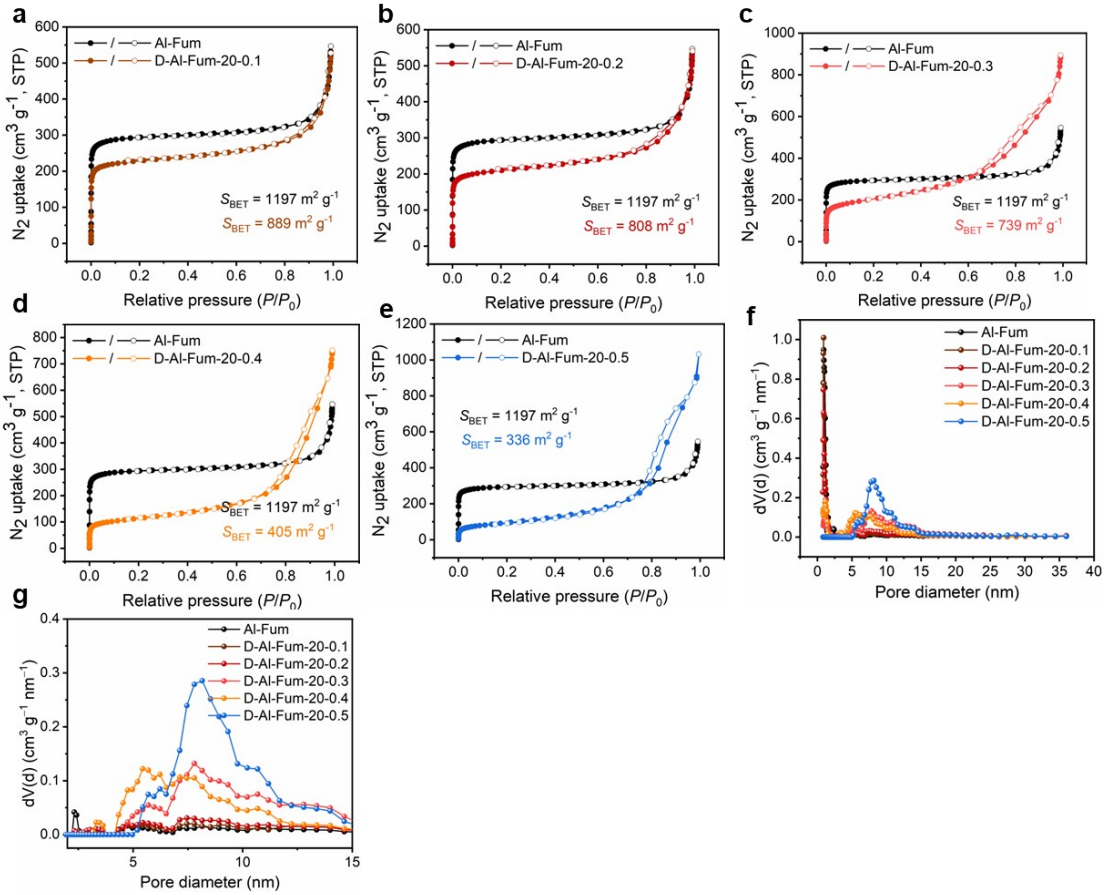

Fig. S11. Nitrogen adsorption-desorption isotherms and corresponding pore size distributions of (a) D-Al-Fum-20-0.1, (b) D-Al-Fum-20-0.2, (c) D-Al-Fum-20-0.3, (d) D-Al-Fum-20-0.4, (e) D-Al-Fum-20-0.5, (f) combined pore size distributions and (g) amplifications of the pore size distributions from 2 nm to 15 nm.

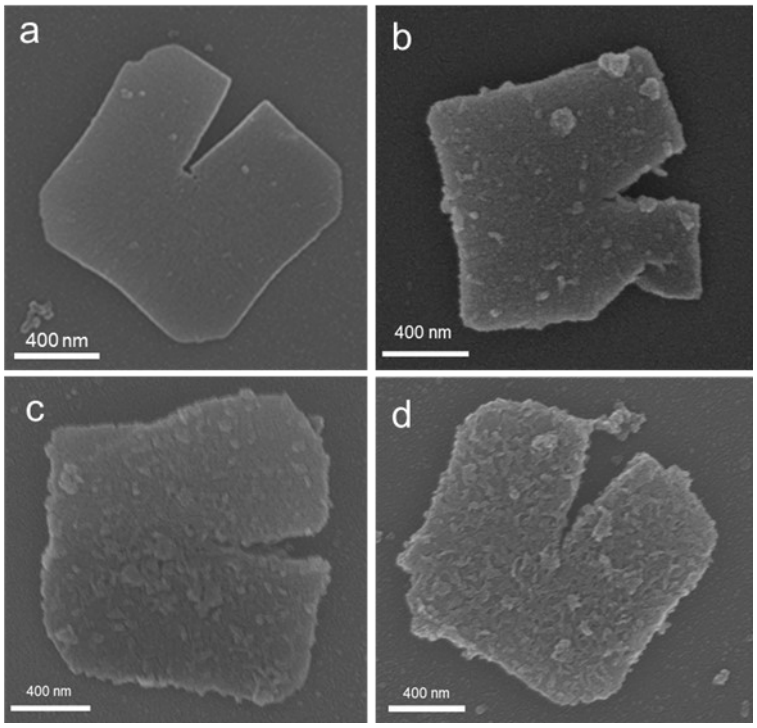

Fig. S12. SEM image of (a) Al-Fum, (b) D-Al-Fum-18-0.1, (c) D-Al-Fum, and (d) D-Al-Fum-18-0.5.

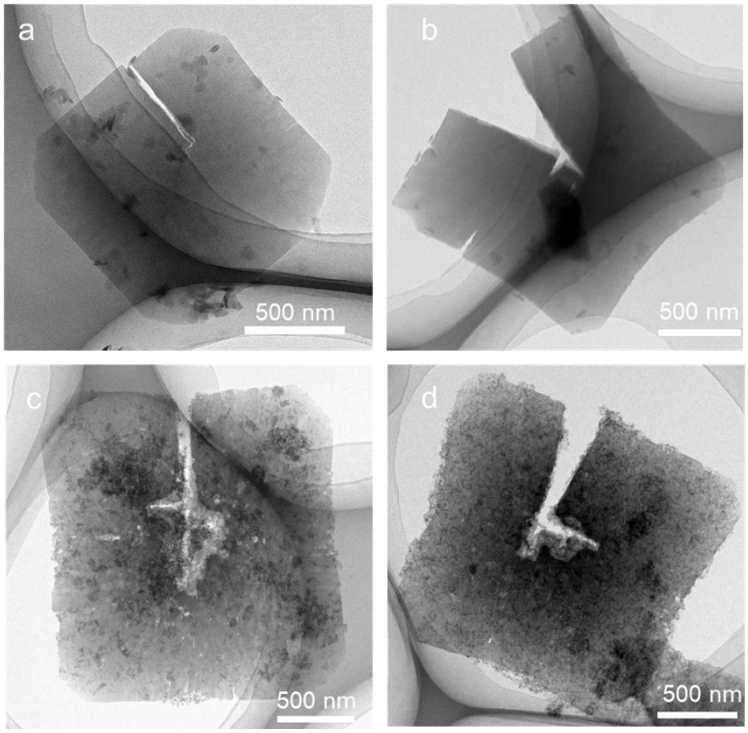

Fig. S13. TEM image of (a) Al-Fum, (b) D-Al-Fum-18-0.1, (c) D-Al-Fum, and (d) D-Al-Fum-18-0.5.

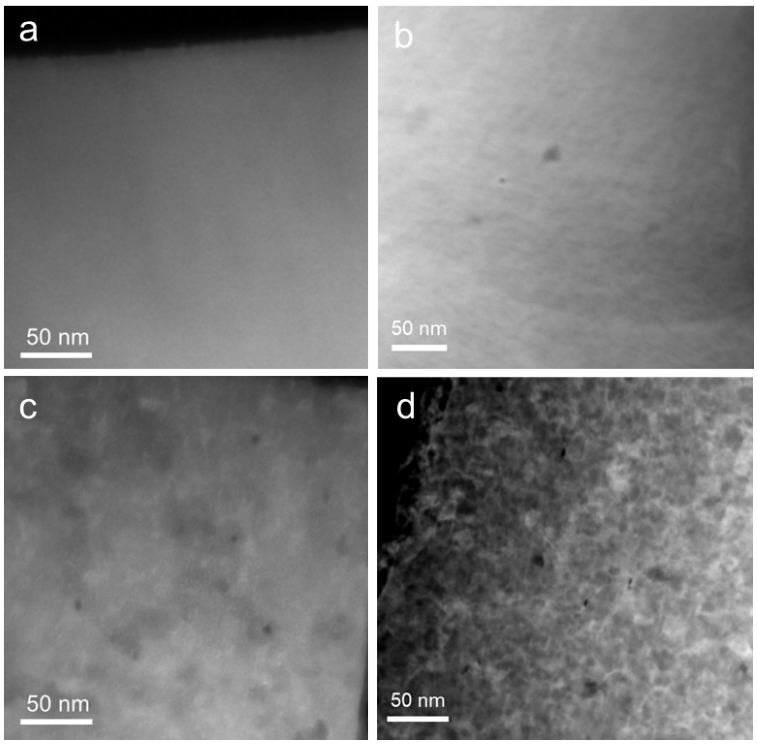

Fig. S14. HAADF-STEM image of (a) Al-Fum, (b) D-Al-Fum-18-0.1, (c) D-Al-Fum, and (d) D-Al-Fum-18-0.5.

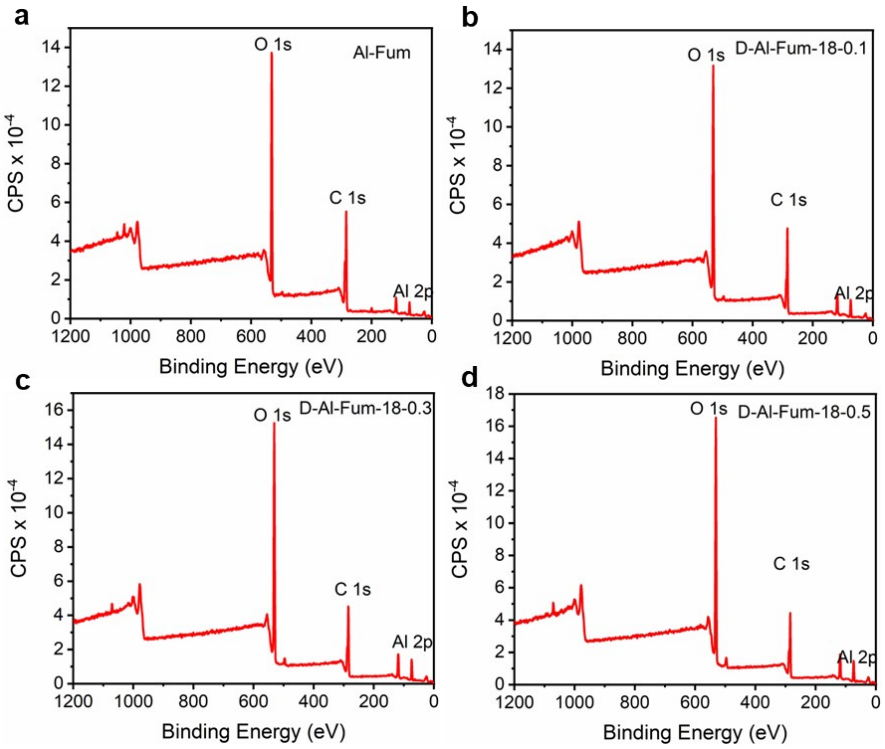

Fig. S15. XPS full spectra of (a) Al-Fum, (b) D-Al-Fum-18-0.1, (c) D-Al-Fum-18-0.3 and (d) D-Al-Fum-18-0.5.

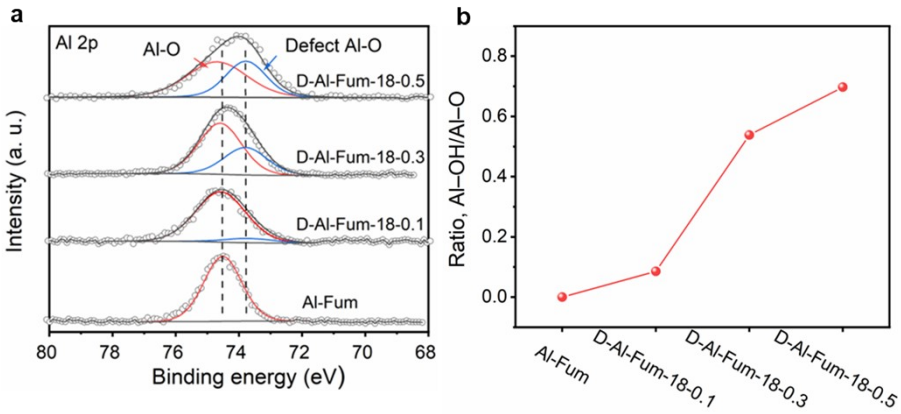

Fig. S16. (a) XPS Al 2p orbital analysis of Al-Fum, D-Al-Fum-18-0.1, D-Al-Fum-18-0.3 and D-Al-Fum-18-0.5. (b) Ratio of the peak intensity of Al-OH and Al-O.

2. Static water adsorption test

Table S4. Comparison of the water adsorption performance of Al-Fum and D-Al-Fum across varying pressure conditions.

P/P_0	Water uptake (Al-Fum, $cm^3 g^{-1}$)	Water uptake (D-Al-Fum, $cm^3 g^{-1}$)	Improvement fold
0.1	8	59	7.3
0.2	22	80	3.6
0.3	457	539	1.18
0.4	493	613	1.24
0.5	501	636	1.27
0.6	510	662	1.30
0.7	521	694	1.33
0.8	536	751	1.40
0.9	579	892	1.54
1.0	827	1150	1.39

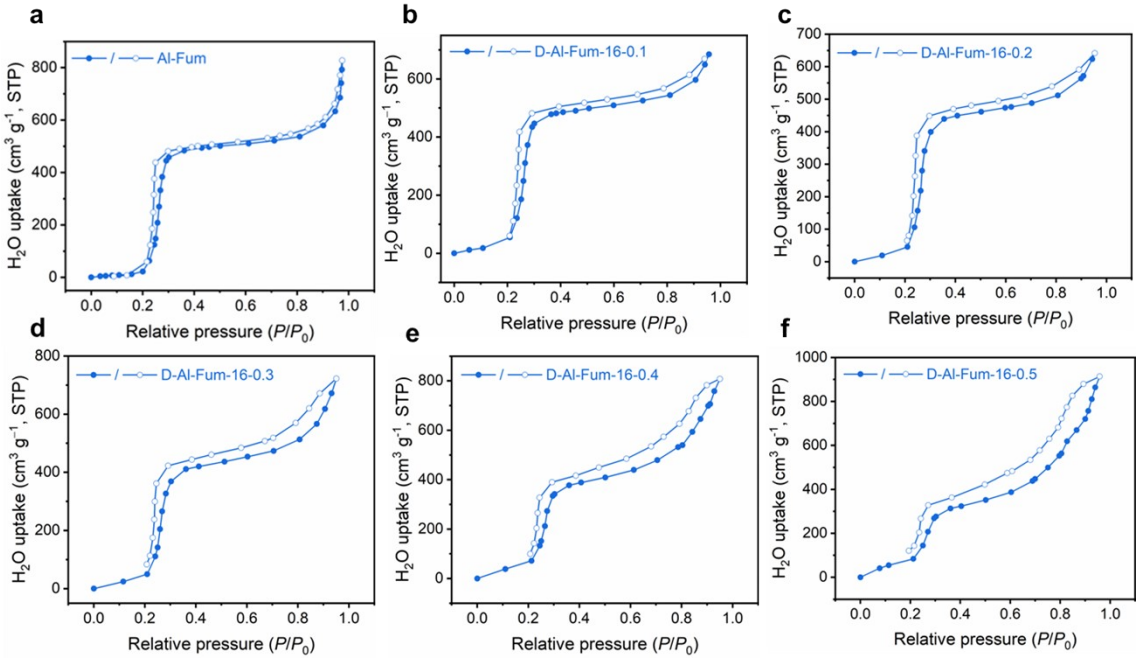

Fig. S17. Water sorption isotherms of (a) Al-Fum, (b) D-Al-Fum-16-0.1 (the degree of ligand loss is 0.07), (c) D-Al-Fum-16-0.2 (the degree of ligand loss is 0.26), (d) D-Al-Fum-16-0.3 (the degree of ligand loss is 0.48), (e) D-Al-Fum-16-0.4 (the degree of ligand loss is 0.62), and (f) D-Al-Fum-16-0.5 (the degree of ligand loss is 0.67) at 298 K.

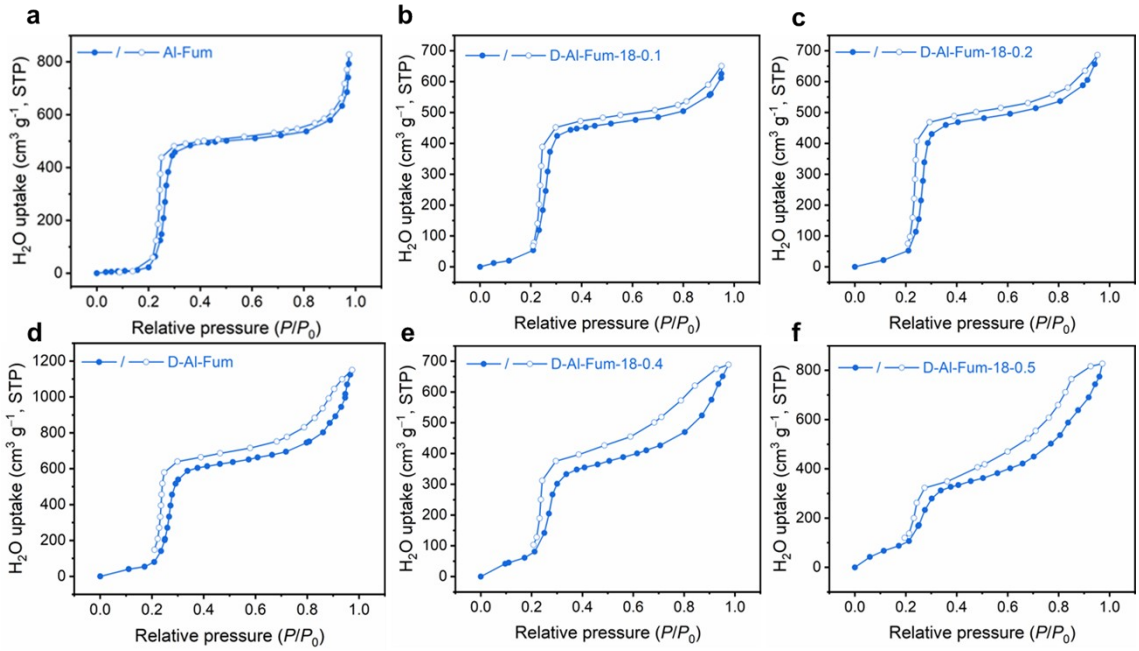

Fig. S18. Water sorption isotherms of (a) Al-Fum, (b) D-Al-Fum-18-0.1 (the degree of ligand loss is 0.11), (c) D-Al-Fum-18-0.2 (the degree of ligand loss is 0.14), (d) D-Al-Fum-18-0.3 (the degree of ligand loss is 0.51), (e) D-Al-Fum-18-0.4 (the degree of ligand loss is 0.68), and (f) D-Al-Fum-18-0.5 (the degree of ligand loss is 0.79) at 298 K.

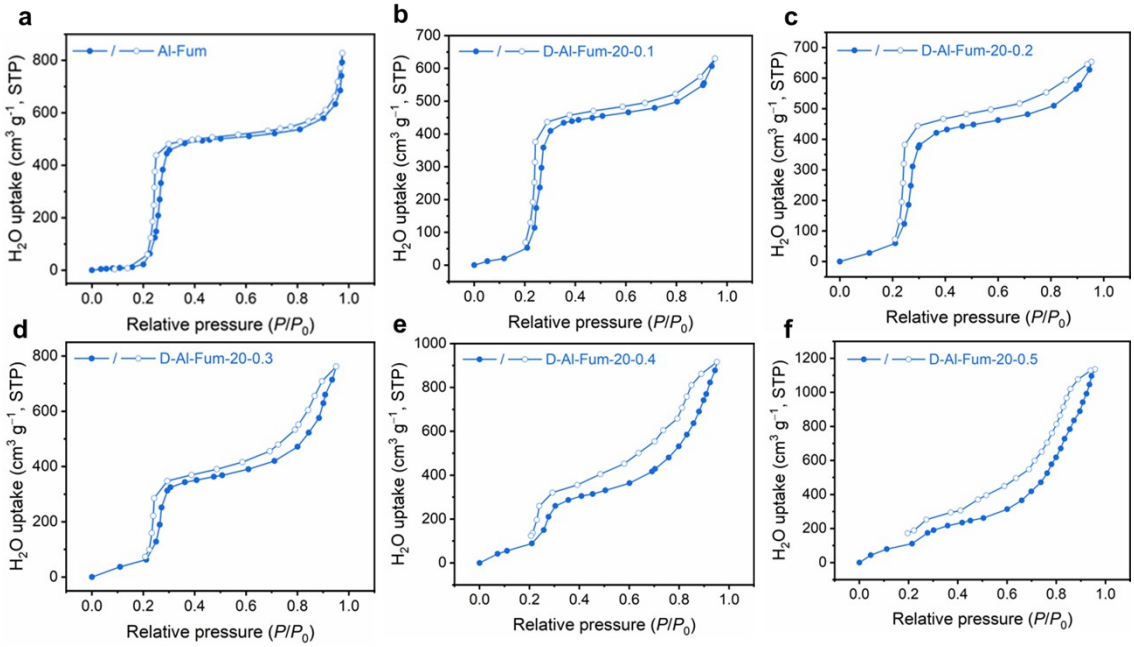

Fig. S19. Water sorption isotherms of (a) D-Al-Fum-20-0.1 (the degree of ligand loss is 0.56), (b) D-Al-Fum-20-0.2 (the degree of ligand loss is 0.59), (c) D-Al-Fum-20-0.3 (the degree of ligand loss is 0.69), (d) D-Al-Fum-20-0.4 (the degree of ligand loss is 0.75), and (e) D-Al-Fum-20-0.5 (the degree of ligand loss is 0.87) at 298 K.

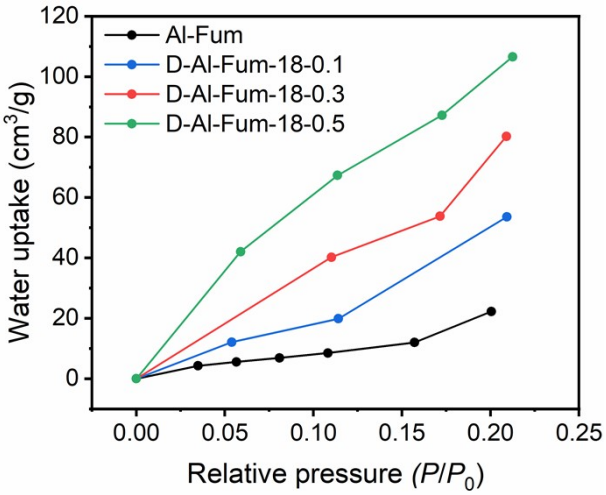

Fig. S20. Water sorption isotherms of Al-Fum (black), D-Al-Fum-18-0.1 (blue), D-Al-Fum-18-0.3 (red), and D-Al-Fum-18-0.5 (green)at P/P_0=0.0 to 0.2.

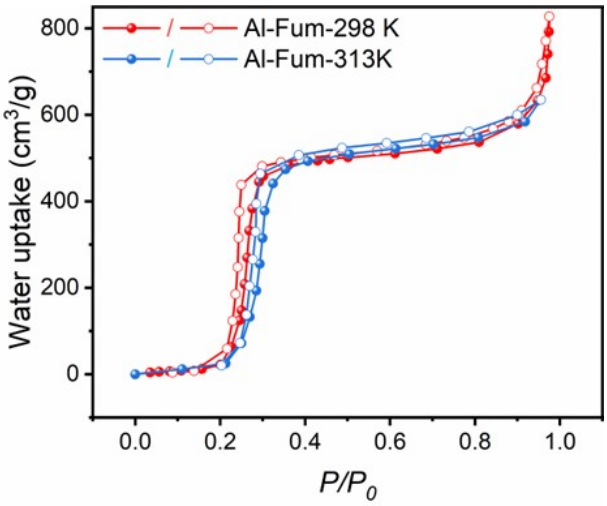

Fig. S21. The water sorption isotherms of Al-Fum at 298 K and 313 K.

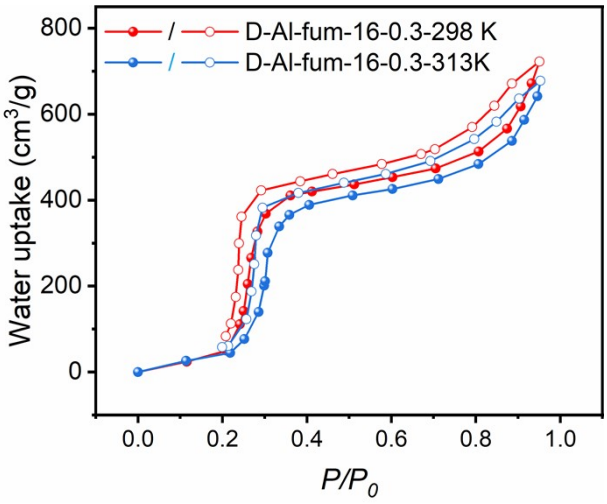

Fig. S22. The water sorption isotherms of D-Al-Fum-16-0.3 at 298 K and 313 K.

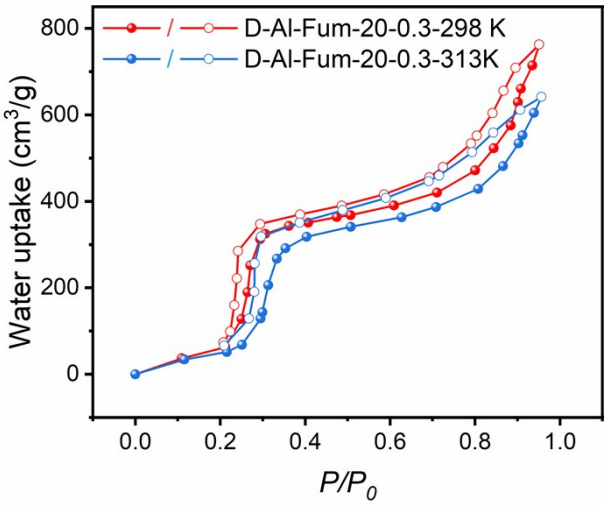

Fig. S23. The water sorption isotherms of D-Al-Fum-20-0.3 at 298 K and 313 K.

Table S5. The comparison of the water adsorption properties of defective samples at low pressure (P/P_0 = 0.2).

Sample	Water uptake (P/P0=0.2, $cm^3\ g^{-1}$)	Improvement fold
Al-Fum	22.3	0
D-Al-Fum-16-0.3	60.2	1.7
D-Al-Fum-20-0.3	62.7	1.8
D-Al-Fum-18-0.1	53.6	1.4
D-Al-Fum-18-0.5	106.6	3.8

3. Dynamic water adsorption test

Note S2:

Water adsorption rate calculation method.

The adsorption rate, denoted as:

$$V = \frac{A_C}{t}$$

The V is defined as the ratio of the adsorption capacity (A_c) of water molecules to the adsorption time (t), where A_c is measured in mg g^{-1}, t in minutes (min), and V in mg g^{-1} min^{-1}.

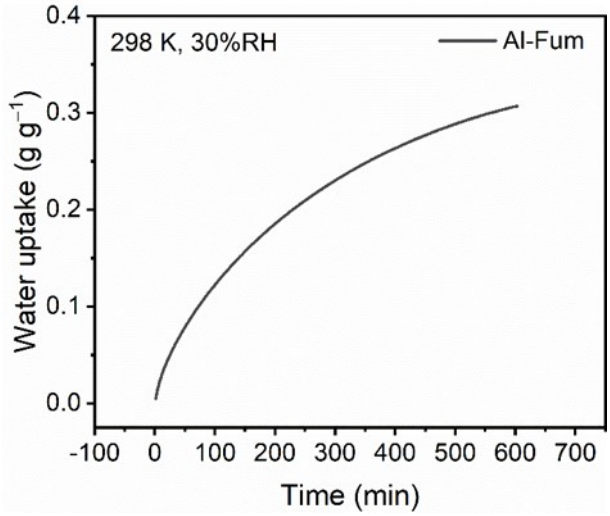

Fig. S24. At 30% R.H airflow, dynamic performance of water adsorption (298 K) for Al-Fum for 600 minutes.

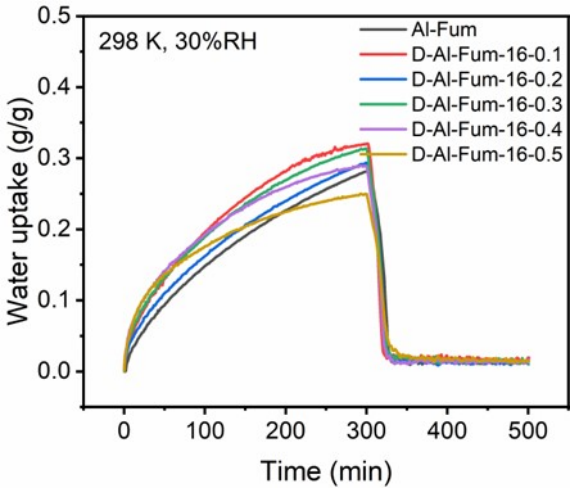

Fig. S25. At 30% R.H airflow, dynamic performance of water adsorption (298 K) for Al-Fum, D-Al-Fum-16-0.1, D-Al-Fum-16-0.2, D-Al-Fum-16-0.3, D-Al-Fum-16-0.4, and D-Al-Fum-16-0.5.

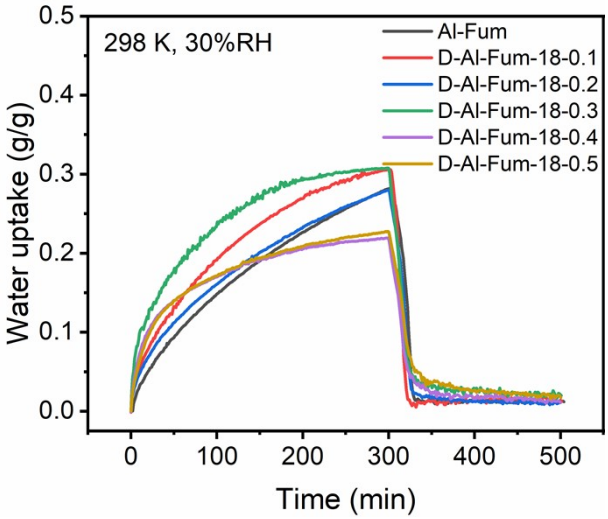

Fig. S26. At (a) 30% R.H airflow, dynamic performance of water adsorption (298 K) for Al-Fum, D-Al-Fum-18-0.1, D-Al-Fum-18-0.2, D-Al-Fum-18-0.3, D-Al-Fum-18-0.4 and D-Al-Fum-18-0.5.

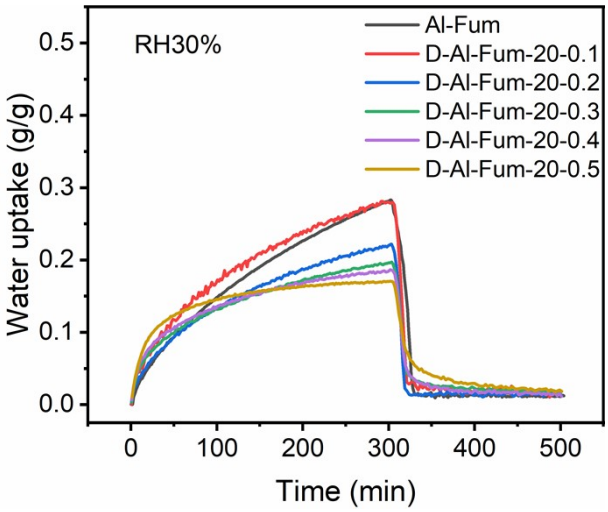

Fig. S27. At (a) 30% R.H airflow, dynamic performance of water adsorption (298 K) for Al-Fum, D-Al-Fum-20-0.1, D-Al-Fum-20-0.2, D-Al-Fum-20-0.3, D-Al-Fum-20-0.4 and D-Al-Fum-20-0.5.

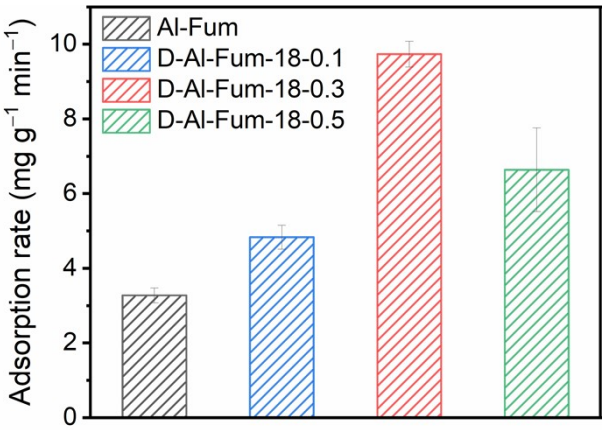

Fig. S28. Dynamic water adsorption rates of samples with different etching concentration.

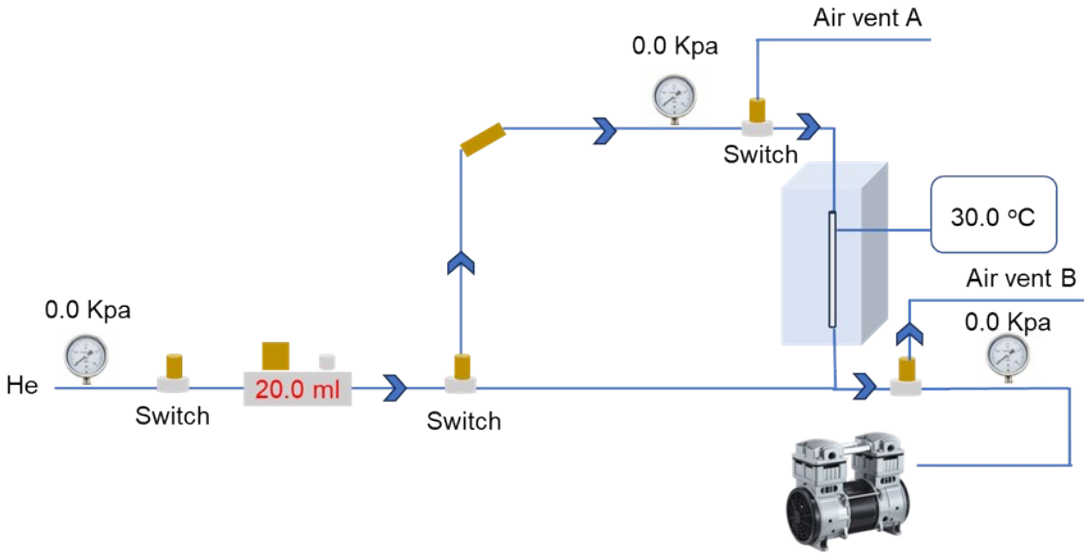

Fig. S29. Schematic representation of the He gas breakthrough apparatus. A penetration column with a specified length-to-diameter ratio of 40:1 was utilized, and 15 mg of sample was loaded, maintaining a column height of 6 mm. Prior to testing, the samples were fully activated at 120°C. Helium gas flow rates were systematically adjusted to 2, 5, 10, 15, 20, 25 and 30 mL min^{-1}, and the pressure drop across the column was measured after stabilization of the pressure at the adsorption bed inlet.

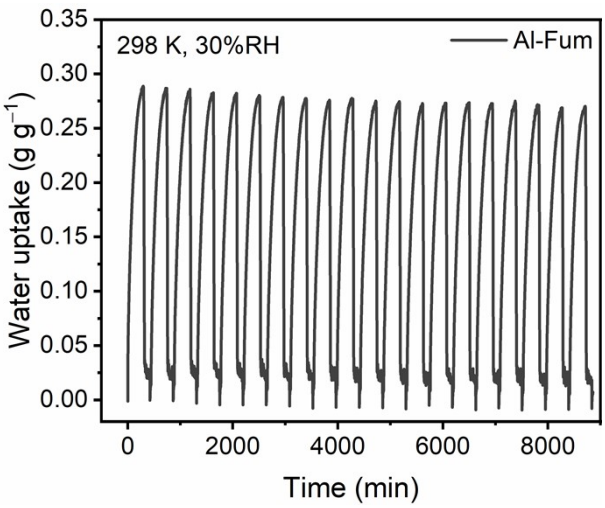

Fig. S30. Cycling stability of Al-Fum at 298 K, 30% RH.

The water adsorption capacity of Al-Fum decreased slightly after 20 cycles compared to D-Al-Fum. This decrease may be attributed to the inherent microporous structure of Al-Fum, which likely impedes the desorption of certain water molecules, thereby occupying adsorption sites and leading to reduced cycling performance.

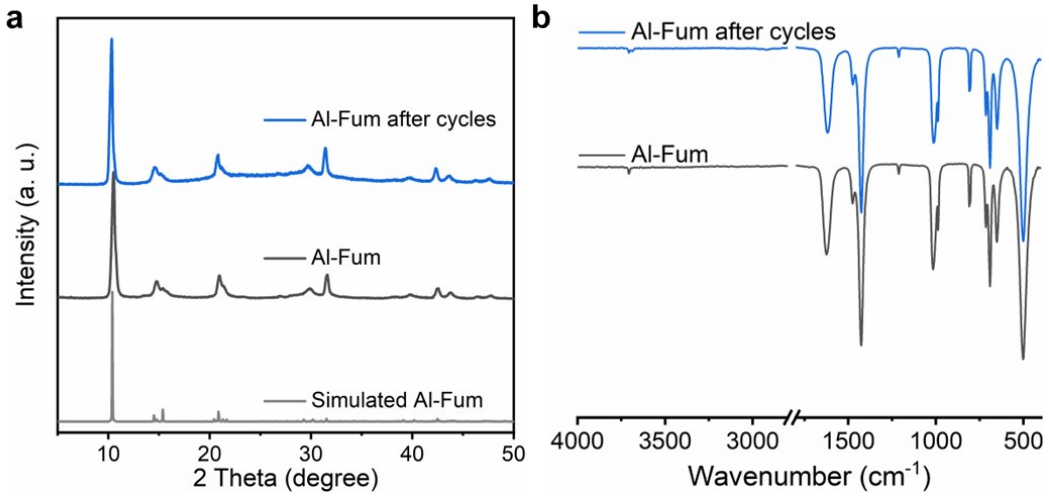

Fig. S31. (a) PXRD pattern and (b) FT-IR spectrum of Al-Fum after 20 adsorption-desorption cycles.

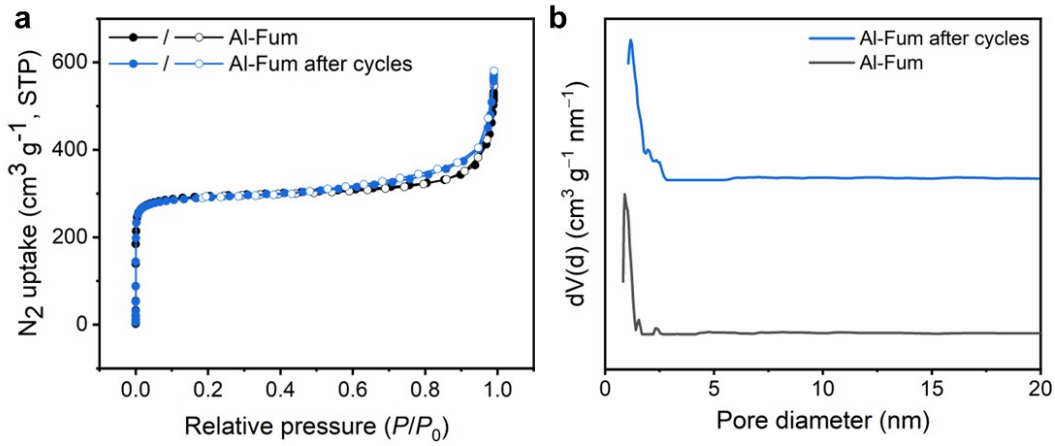

Fig. S32. (a) N_2 adsorption-desorption isotherms and (b) pore size distribution analysis of Al-Fum after 20 adsorption-desorption cycles.

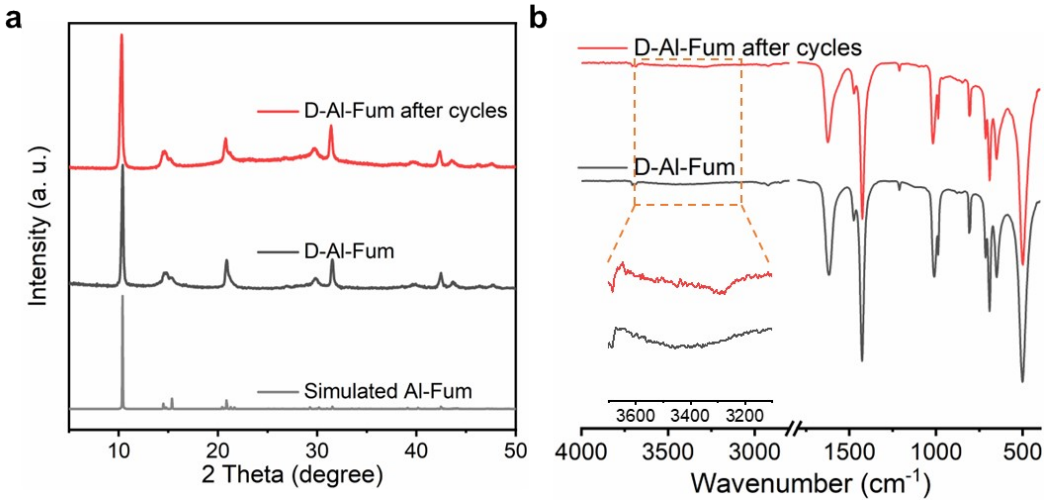

Fig. S33. (a) PXRD pattern and (b) FT-IR spectrum of D-Al-Fum after 20 adsorption-desorption cycles.

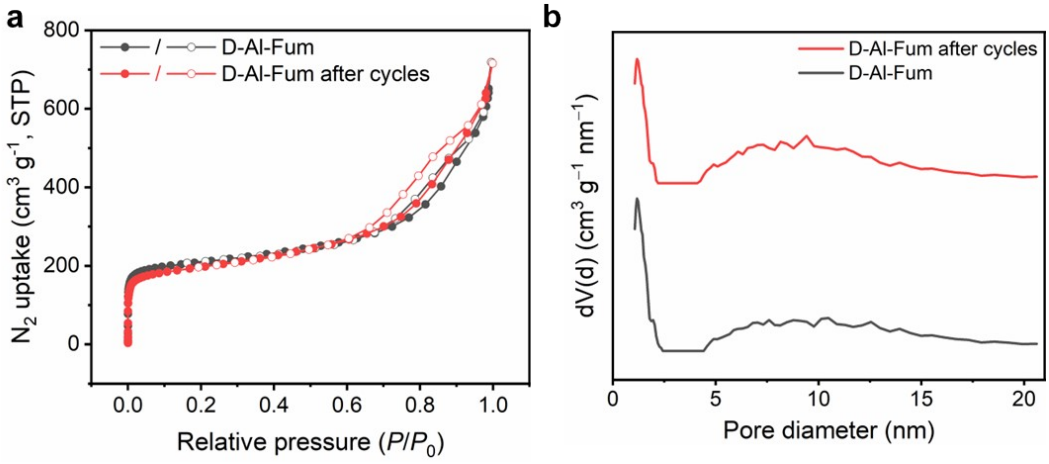

Fig. S34. (a) N_2 adsorption-desorption isotherms and (b) pore size distribution analysis of D-Al-Fum after 20 adsorption-desorption cycles.

4. Water vapor sorption measurement setup

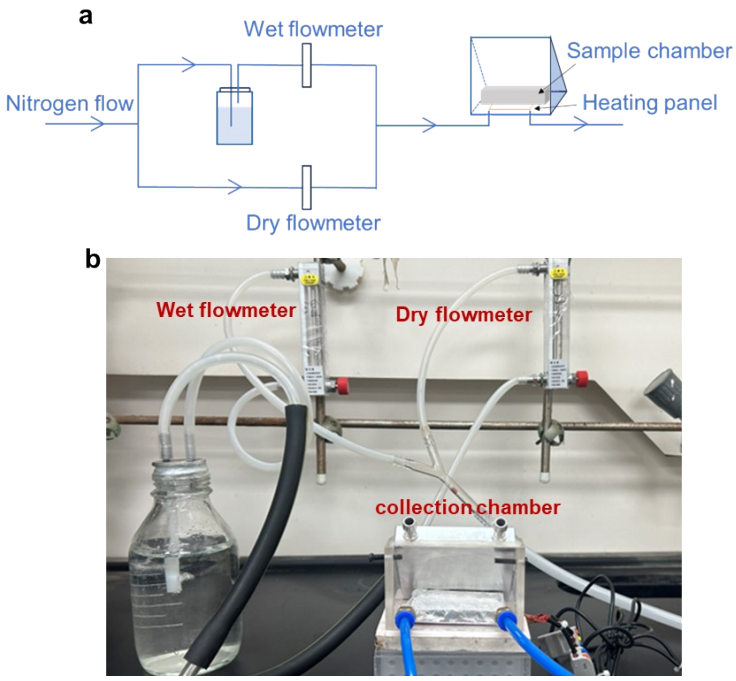

Fig. S35. Water vapor sorption measurement setup. (a) Setup schematic, (b) Setup photograph.

Note S3：

The home-made water collection device comprises three primary components: a water vapor generating unit, an adsorption and desorption chamber and a sample adsorption bed. The water vapor is generated by mixing dry and wet N_2, with their respective flow rates precisely regulated by rotameters. In this experiment, conducted at 30% relative humidity, the wet airflow is maintained at 120 mL min^{-1}, the dry airflow at 280 mL min^{-1}, and the total flow rate of the mixed gas is 400 mL min^{-1}. The adsorption-desorption chamber is equipped with both an air inlet and outlet to facilitate air exchange. A built-in heating plate, powered by a flexible polyimide heater (25 mm × 50 mm, 12 V, 7 W), enables precise control of the desorption temperature. The inner wall of one side is composed of hollow metal plate, designed to condense water vapor and collect it as liquid via a condensate water channel. A water collector is positioned beneath the inner wall to capture the condensed liquid. The sample adsorption bed is constructed using aluminum foil to securely hold the powder sample.

During the desorption process, noticeable water mist was observed within the test chamber. Upon completion of desorption, the released water was collected and weighed, yielding a calculated water production of 0.15 g g^{-1}.

5. Theoretical calculation

Density functional theory (DFT) calculations

We have employed the VASP to perform all the spin-polarized density functional theory (DFT) calculations within the generalized gradient approximation (GGA) using the Perdew-Burke-Ernzerhof (PBE) formulation. We have chosen the projected augmented wave (PAW) potentials to describe the atomic and take valence electrons into account using a plane wave basis set with a kinetic energy cutoff of 520 eV. Partial occupancies of the Kohn−Sham orbitals were allowed using the Gaussian smearing method and a width of 0.05 eV. The convergence criteria were set to 0.01 eV $Å^{-1}$ and 10^{-6} eV for the residual force and energy during structure relaxation. The van der Walls interactions was considered by the DFT dispersion correction (DFT-D). The Brillouin zone was sampled by a 2×2×1 k-points grid for the structure optimizations. In all calculations, van der Waals (vdW) interactions were accounted for at the D3 level.

The absorption energy was calculated using the following equation, $\Delta E_{H2O} = E_{surf-H2O} - E_{surf} - E_{H2O}$, where $E_{surf-H2O}$ and E_{surf} are the total energies of the surface covered with and without adsorbed molecule, and E_{H2O} is the energy of free absorbed molecule.

Molecular dynamic (MD) simulations

For MD simulations, all the MD simulation were conducted by the Large-scale Atomic/Molecular Massively Parallel Simulator (LAMMPS) from Sandia National Laboratories. The basic concept behind it was to iterate Newton's law of motion through many timesteps. It supported the force fields and gives reliable results. Prior to calculation, the structures of Al-Fum and defective Al-Fum were optimized to achieve minimized energy configurations. The MOFUFF force field was applied for the framework, while the SPC/E force field was used for water molecules. Molecular dynamics simulations were conducted in the NVT ensemble at 298 K for 5 ns, using a model with dimensions of 26 × 12 × 12 nm and 7,000 water molecules.The diffusion coefficients of water were calculated by using the Einstein equation, which were given by：

$$MSD_i = < \left| \underset{r_i}{\rightarrow}(t) - \underset{r_i}{\rightarrow}(0) \right|^2 > (i = x,y,z)$$

$$D_{MSD} = \lim_{x \to \infty} \frac{1}{2nt} < \left| \underset{r_i}{\rightarrow}(t) - \underset{r_i}{\rightarrow}(0) \right|^2 >$$

Where MSD_i is the mean square displacement (MSD) equation; *r(t)* represents position of the water molecular mass center at time t; $< >$ represents the average value of displacement of all water molecules in the system from initial time to time t; D_{MSD} means the diffusion coefficient obtained by the time variability of MSD by the Einstein relation; *n* represents the calculated spatial dimension. Note that in the calculations we only consider the water molecules inside the confined space. Thus, the diffusion coefficient is only obtained from the 2 ns of the MSD, as shown in Figure S40.

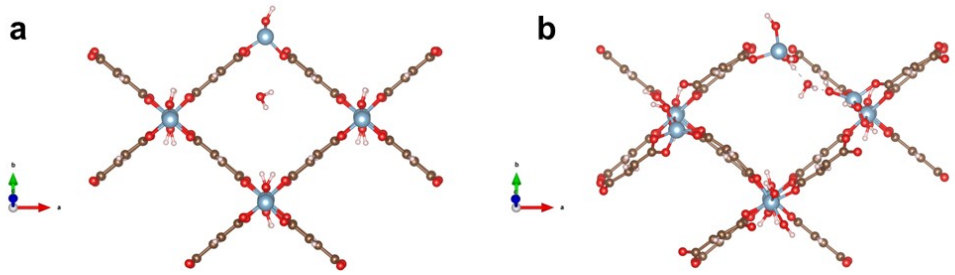

Fig. S36. Density functional theory (DFT) calculations were performed to determine the adsorption energy of water molecules at equivalent sites in Al-Fum (a) and defect Al-Fum (b). While water molecules in Al-Fum migrated to the energetically favorable position after optimization, in defective Al-Fum, the presence of Al–OH groups at defect sites facilitated hydrogen bonding, causing water molecules to preferentially localize near these defect regions.

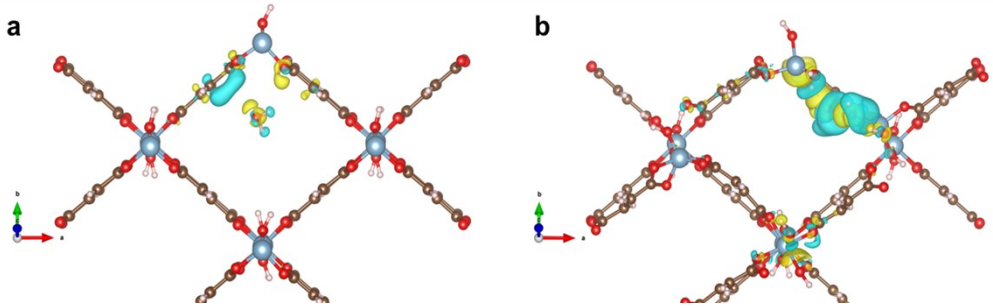

Fig. S37. Differential charge calculation of (a) Al-Fum and (b) defect Al-Fum.

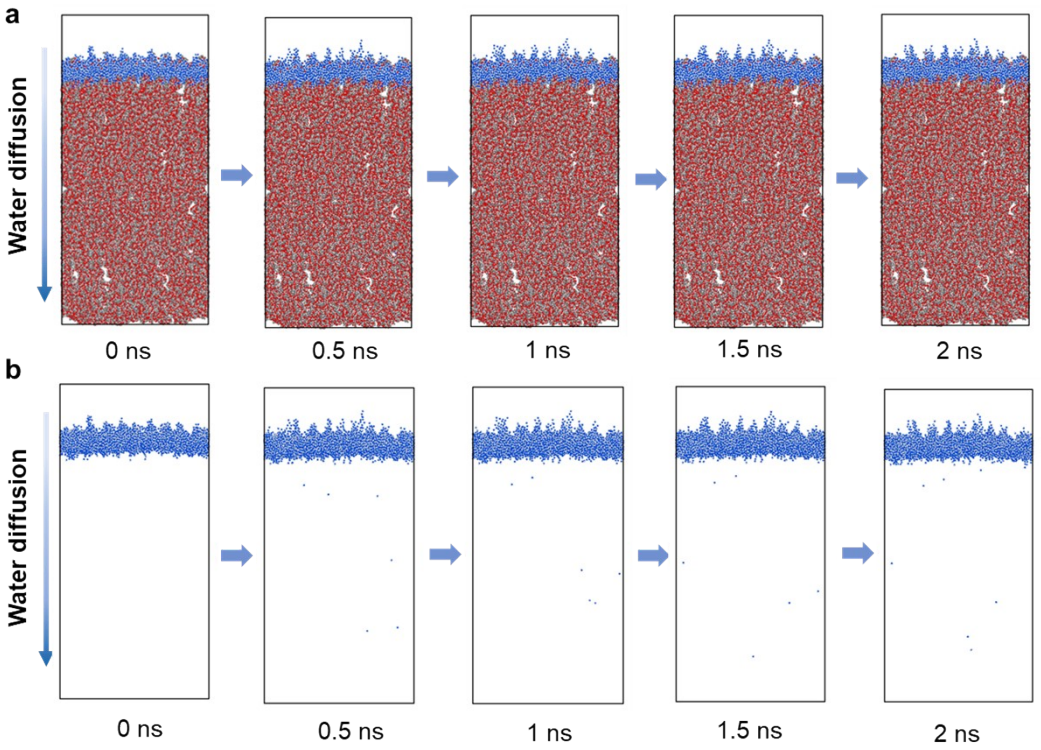

Fig. S38. Molecular dynamics simulation snapshot of water molecule diffusion. (a) Diffusion process of water molecules in Al-Fum structure. (b) diffusion trajectories of water molecules.

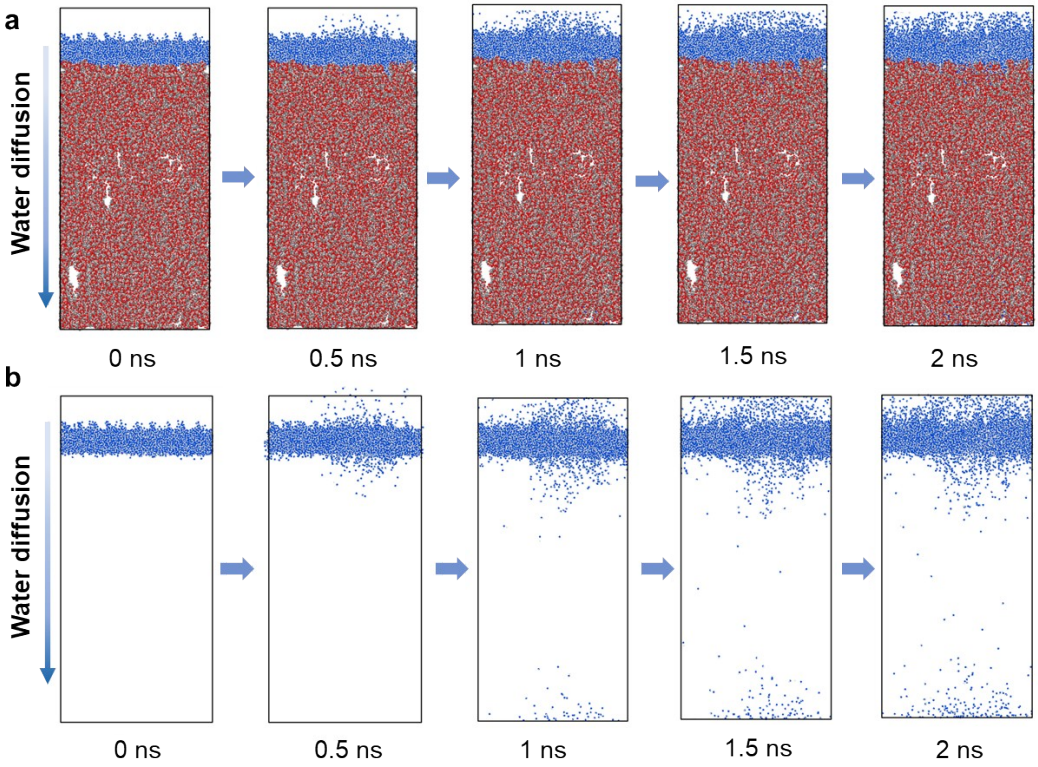

Fig. S39. Molecular dynamics simulation snapshot of water molecule diffusion. (a) Diffusion process of water molecules in defective Al-Fum structure. (b) diffusion trajectories of water molecules.

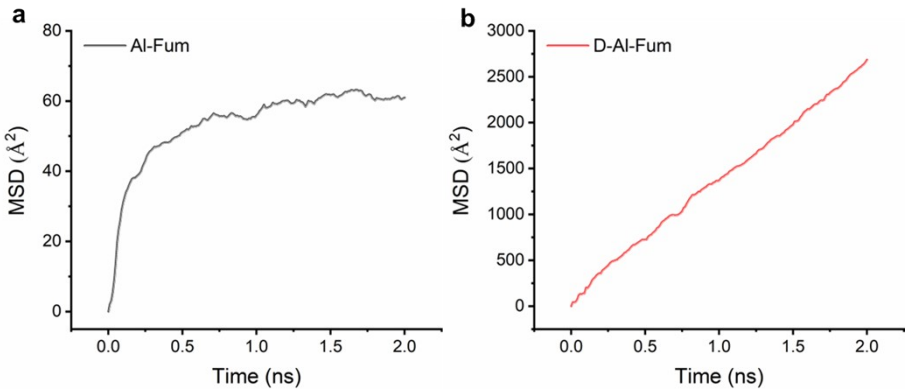

Fig. S40. The diffusion coefficients of water molecules in (a) Al-Fum and (b) defect Al-Fum were calculated using molecular dynamics simulations (MD), providing insights into the impact of structural defects on water transport behavior.

References：

1. I. A. Lázaro, *Eur. J. Inorg. Chem.*, 2020, **2020**, 4284-4294.